

# Influence of rotational instability on the polarization structure of SrTiO<sub>3</sub>

Yanpeng Yao and Huaxiang Fu

*Department of Physics, University of Arkansas, Fayetteville, AR 72701, USA*

(Dated: November 19, 2018)

## Abstract

The  $k$ -space polarization structure and its strain response in SrTiO<sub>3</sub> with rotational instability are studied using a combination of first-principles density functional calculations, modern theory of polarization, and analytic Wannier-function formulation. (1) As one outcome of this study, we rigorously prove—both numerically and analytically—that folding effect exists in polarization structure. (2) After eliminating the folding effect, we find that the polarization structure for SrTiO<sub>3</sub> with rotational instability is still considerably different from that for non-rotational SrTiO<sub>3</sub>, revealing that polarization structure is sensitive to structure distortion of oxygen-octahedra rotation and promises to be an effective tool for studying material properties. (3) Furthermore, from polarization structure we determine the microscopic Wannier-function interactions in SrTiO<sub>3</sub>. These interactions are found to vary significantly with and without oxygen-octahedra rotation.

PACS numbers: 77.80.-e, 77.84.-s, 77.22.Ej

## I. INTRODUCTION

Materials with perovskite or perovskite-based structures have attracted wide attention for their varieties of properties in ferroelectricity, magnetism, superconductivity, etc. In these perovskite solids, an important class of structural distortions that deviate them from ideal (cubic) perovskites is the rotation of the oxygen octahedra, which may considerably alter the physical and chemical properties of materials. For instance, rotation of oxygen octahedra in incipient ferroelectric  $\text{SrTiO}_3$  was found to couple strongly with tetragonal strain, and consequently, affect significantly the structural and dielectric behaviors below 105K.[1, 2] Octahedral rotation also plays a key role in improper ferroelectrics such as  $\text{YMnO}_3$ , where structural instability due to zone-boundary phonon mode couples with electric polarization[3], and this coupling was recently shown to exhibit an interesting absence of critical thickness in improper-ferroelectric ultrathin films.[4] On magnetism, Mazin and Singh have revealed that one main reason responsible for the drastically different magnetic properties in two chemically similar compounds  $\text{CaRuO}_3$  and  $\text{SrRuO}_3$  (where  $\text{CaRuO}_3$  is paramagnetic, but  $\text{SrRuO}_3$  is ferromagnetic) consists in a larger rotation angle of  $\text{RuO}_6$  octahedra in  $\text{CaRuO}_3$ . [5] Similarly, Fang and Terakura found that perovskite superconductor  $\text{Sr}_2\text{RuO}_4$  could be turned from non-magnetic to ferromagnetic by simply increasing the rotation angle of the  $\text{RuO}_6$ . [6] Recently, Ray and Waghmare have shown that rotation is the predominant structural instability in a series of biferroics ( $\text{LuCrO}_3$ ,  $\text{YCrO}_3$ ,  $\text{LaCrO}_3$ ,  $\text{BiCrO}_3$ , and  $\text{YCrO}_3$ ), and is closely correlated with their magnetic properties.[7] Based on the facts that (1) rotation of oxygen octahedra affects various material properties, and (2) the oxygen-octahedra rotation is common, understanding of the physics caused by oxygen rotation is thus important.

The modern theory of polarization[8, 9] has become important in quantitatively determining the electric and dielectric properties of materials within first-principles density functional calculations. According to this theory[8, 9], the change of electric polarization is a physically meaningful quantity and the electronic contribution is determined by an integration of the geometric phase of the occupied multi-fold electron Bloch wavefunctions. Based on the modern theory of polarization, Yao and Fu recently introduced the concept of “polarization structure” [10] which may provide a new scheme to study the electronic properties of dielectric materials, and they went on to formulate a theory using localized Wannier func-

tions to investigate the polarization dispersion structure of ferroelectrics with spontaneous polarization. More specifically, polarization structure describes the electronic phase angle  $\phi$  as a function of  $\vec{k}_\perp$  point which lies on a  $\vec{k}$ -plane perpendicular to the direction of the considered polarization component. At each  $\vec{k}_\perp$ , the phase angle is determined by the electron wavefunctions as[8, 9]

$$\phi(\vec{k}_\perp) = i \sum_{n=1}^M \int_0^{G_\parallel} d\vec{k}_\parallel \langle u_{n\vec{k}} | \frac{\partial}{\partial k_\parallel} | u_{n\vec{k}} \rangle , \quad (1)$$

where subscripts  $\parallel$  and  $\perp$  indicate, respectively, the directions parallel and perpendicular to the direction of the polarization.  $u_{n\vec{k}}$  is the Bloch part of electron wave function, and  $M$  is the number of occupied bands. As significant as electronic band structure, polarization structure reveals how individual strings of different  $\vec{k}_\perp$ s contribute to the electronic polarization, which thus offers microscopic insight on the polarization properties. Polarization structure can be changed by applied electric fields, in a similar spirit as electronic state in band structure can be changed by photoexcitation. More discussions on the importance of the polarization structure were given in Ref.10. It was also shown that the polarization structure is determined by the interaction among Wannier functions in neighboring cells.[10] Polarization structure of a dielectric system may thus enable scientists to study the microscopic interaction among Wannier functions in real space, which is of fundamental relevance in revealing material properties.

In this work we address a topic which concerns both the rotational instability of oxygen octahedra and polarization structure, by investigating how the polarization dispersion structure in ferroelectric perovskites is influenced by oxygen rotation. We will use SrTiO<sub>3</sub> (ST) as an example. ST is known as an incipient ferroelectric, which exhibits no polarization at the strain-free ground state but is ready to develop a polarization under small external strains.[11] It was observed experimentally that unstrained ground state of ST has a nonzero oxygen-octahedra rotation around the (001) direction. Later, we will see from our numerical simulations that by applying in-plane compressive strain, the rotation angle in ST increases and the structure with oxygen rotation remains to be the most stable ground state as the strain is small or moderate. But at large strains, the tetragonal phase of zero rotation becomes more stable. Comparing SrTiO<sub>3</sub> (with oxygen rotation) with PbTiO<sub>3</sub> (of no oxygen rotation), one anticipates both the atom-atom interaction and electron wave functions to be altered in two materials. Since the polarization structure is determined by electron wave-

functions and their interaction, it is thus of interest to study how the polarization structure changes as a result of the octahedral rotation. It is worth pointing out that the influence of rotational instability on the polarization structure has not been studied before [10], and turns out to offer interesting new knowledge on the phase contribution at individual  $\vec{k}_\perp$  points as well as on microscopic interaction.

The purpose of this work is three folds: (i) To determine and reveal how the polarization structure may look like in ferroelectrics with rotation instability, using first-principles density functional calculations; (ii) By comparing the polarization structure in SrTiO<sub>3</sub> with oxygen rotation (labeled as R-SrTiO<sub>3</sub>) with the counterpart in non-rotational SrTiO<sub>3</sub> (to be denoted as NR-SrTiO<sub>3</sub> where the oxygen-octahedral rotation is deliberately suppressed by symmetry constraint), we intend to investigate the effect of rotational instability on the formation of polarization dispersion structure; (iii) Since octahedral rotation couples with, and can be changed by, inplane strains, we thus would like to explore how the polarization structure in perovskites with rotation instability may be modified by the inplane strain.

The content of this paper is organized as following. In Sec.II we describe the computational methods used in this study, along with a brief result on the structural responses in R-SrTiO<sub>3</sub> and NR-SrTiO<sub>3</sub>. In Sec.III we present the polarization structures for R-SrTiO<sub>3</sub> and NR-SrTiO<sub>3</sub>, and identify the differences and similarities between these polarization structures. Two main reasons contributing to the differences are revealed. In addition, analytical formulation is also made in Sec.III to deduce from polarization dispersion the microscopic interaction among Wannier functions. We find that the 3rd nearest neighbor (3NN) approximation is necessary in order to yield an accurate polarization structure for NR-SrTiO<sub>3</sub> under large inplane strains. Based on our analytical formulation and numerical simulation, we also describe a renormalization-group scheme to determine the higher-order interactions between Wannier functions. Sec.IV summarizes the results of this work.

## II. METHODS AND STRUCTURAL RESPONSE

We use first-principles density-functional theory (DFT) within local density approximation (LDA) [12] to determine cell parameters and internal atomic positions in zero-strained SrTiO<sub>3</sub> as well as in SrTiO<sub>3</sub> under different compressive in-plane strains. More specifically, for a given inplane lattice constant  $a$ , both the out-of-plane lattice constant  $c$  and atomic

locations are optimized by minimizing the total energy and forces. For the optimization of atomic positions, residual forces on each atom are required to be smaller than  $10^{-3}$  eV/Å. Effects of nuclei and core electrons are replaced by Troullier-Martins norm-conserving type of pseudopotentials[13]; semi-core states Ti 3s and 3p are treated as valence states for better accuracy. Bloch wave functions in solid are expanded using a mixed-basis set consisting of numerical atomic pseudo-orbitals and plane waves.[14] A cutoff energy of 100 Ryd in wavefunction expansion is used for both rotational and non-rotational SrTiO<sub>3</sub> on equal footing, and has been checked to be sufficient. Details on generating pseudopotential, pseudo/all-electron matching radii, and the accuracy checking were described in Ref.[15]. Polarization structure, namely the contribution of a given  $\vec{k}_\perp$  string to the electronic polarization, is calculated according to the equation[8, 9]  $\phi(\vec{k}_\perp) = \text{Im}\{\ln \prod_{j=0}^{J-1} \det(\langle u_{m,k_j} | u_{n,k_{j+1}} \rangle)\}$ , where  $J$  is the number of  $\vec{k}_\parallel$  points along the string. One advantage of this equation over Eq.(1) is that  $\phi(\vec{k}_\perp)$  here does not depend on the arbitrariness of the phases of Bloch  $u_{n\vec{k}}$  wavefunctions at individual  $\vec{k}$  point.

Figure 1(a) and (b) show the top-view of the cell structure for NR-SrTiO<sub>3</sub> without octahedral rotation of 5-atoms each cell, and for R-SrTiO<sub>3</sub> with octahedral rotation of 10-atoms each cell, respectively. In NR-SrTiO<sub>3</sub>, the lattice vectors are  $\vec{a}'_1 = a\vec{i}$ ,  $\vec{a}'_2 = a\vec{j}$ ,  $\vec{a}'_3 = c\vec{k}$ . Biaxial compressive strains are applied in the  $\vec{a}'_1$  and  $\vec{a}'_2$  directions. In R-SrTiO<sub>3</sub>, the lattice vectors are  $\vec{a}_1 = a(\vec{i} - \vec{j})$ ,  $\vec{a}_2 = a(\vec{i} + \vec{j})$ ,  $\vec{a}_3 = c\vec{k}$ . The rotation angle  $\theta$ , as illustrated in Fig.1(b), characterizes the deviation of the oxygen atoms from the non-rotational positions in the  $\vec{a}_1$ - $\vec{a}_2$  plane. In the rest of this section, we will briefly give our results on the optimized structures for NR-SrTiO<sub>3</sub> and R-SrTiO<sub>3</sub> under different inplane strains, since these data could be useful for experiments or other theoretical calculations. The main results on polarization dispersion will be discussed in the next section.

Figure 2(a) gives the total energies per 10 atoms for NR-SrTiO<sub>3</sub> and R-SrTiO<sub>3</sub> at different in-plane  $a$  lattice constants; each curve is obtained by imposing symmetry constraint on the corresponding structure. One main result in Fig.2(a) is that a crossover in the ground-state structure occurs at  $a_c = 3.62\text{Å}$ . When  $a > a_c$ , R-SrTiO<sub>3</sub> has a lower energy than NR-SrTiO<sub>3</sub> and is thus more stable. As  $a$  is below  $a_c$ , NR-SrTiO<sub>3</sub> becomes more stable, and the crystal of strained SrTiO<sub>3</sub> changes from rotational to non-rotational. Meanwhile, we need to point out that at the equilibrium lattice constant  $a_0 = 3.86\text{Å}$ , our LDA simulations yield a rather small energy difference between NR-SrTiO<sub>3</sub> and R-SrTiO<sub>3</sub>, which is on the order of numerical

uncertainty, and does not allow us to tell which structure is more stable. This, however, does not contradict with the fact that R-SrTiO<sub>3</sub> is found more stable in experiments, since LDA calculations can not capture the zero-point quantum fluctuation which is known important in stabilizing the experimentally-observed rotational ground state of incipient SrTiO<sub>3</sub>. On the other hand, since the main purpose of this work is to understand the polarization-structure difference between R-SrTiO<sub>3</sub> and NR-SrTiO<sub>3</sub>, the above uncertainty in the ground-state structure does not affect our purpose of investigating the polarization structure.

The calculated  $c/a$  tetragonality is given in Table I, along with the rotation angle  $\theta$  in R-SrTiO<sub>3</sub>. Under zero strain, both R-SrTiO<sub>3</sub> and NR-SrTiO<sub>3</sub> are found to possess an equilibrium inplane lattice constant of  $a_0=3.86\text{\AA}$ , agreeing well with the experimental value[16] of  $3.90\text{\AA}$  for R-SrTiO<sub>3</sub> at low temperature. For R-SrTiO<sub>3</sub> at  $a_0$ , our theoretical rotation angle is  $\theta=3.25^\circ$ , comparable to the experimental value[17] of  $2.1^\circ$  as well as  $5.5^\circ$  in another theoretical calculation[18]. Under inplane strains, the  $c/a$  ratios are shown in Fig.2(b). One could see that by decreasing  $a$ ,  $c/a$  increases for both NR-SrTiO<sub>3</sub> and R-SrTiO<sub>3</sub>. At small strains ( $a>3.71\text{\AA}$ ),  $c/a$ 's of two structures remain close; however, at large strains ( $a<3.71\text{\AA}$ ),  $c/a$  of NR-SrTiO<sub>3</sub> increases dramatically, and becomes evidently larger than that in R-SrTiO<sub>3</sub>. Interestingly, for the strain range studied here,  $c/a$  of R-SrTiO<sub>3</sub> depends on  $a$  in a rather linear fashion. In contrast, for NR-SrTiO<sub>3</sub>, the  $c/a$  ratio undergoes an obvious slope change around  $a=3.71\text{\AA}$ . Strain-induced total polarization is shown in Fig.2(c), where we see (i) for NR-SrTiO<sub>3</sub>, there is a critical inplane lattice constant  $a \approx 3.82\text{\AA}$ , above which polarization remains null; (ii) However, for R-SrTiO<sub>3</sub>, such a critical inplane lattice constant apparently does not exist, and instead polarization increases almost linearly with the decreasing inplane lattice constant.

The differences between NR-SrTiO<sub>3</sub> and R-SrTiO<sub>3</sub> in the  $c/a$  tetragonality [Fig.2(b)] and in the electric polarization [Fig.2(c)] can be explained microscopically by the ferroelectric atomic off-center displacements, which are shown in Fig.2(d). In NR-SrTiO<sub>3</sub>, atomic displacements of O1 and O2 atoms are small when  $a>3.80\text{\AA}$  and then increases drastically with a notable slope change as  $a$  is below  $3.80\text{\AA}$ , which causes the sharp rise of electric polarization in Fig.2(c). On the other hand, in R-SrTiO<sub>3</sub> the off-center displacements of O1 and O2 vary rather linearly with the decreasing inplane lattice constant, without significant change in slope. At  $a=3.59\text{\AA}$ , the oxygen displacements in NR-SrTiO<sub>3</sub> are more than two times as those in R-SrTiO<sub>3</sub>.

### III. POLARIZATION STRUCTURE

#### A. Comparison on polarization dispersions

We now present and discuss the polarization structures for SrTiO<sub>3</sub> with and without oxygen-octahedra rotation, in particular the similarity and difference between them. Under zero strain, both NR-SrTiO<sub>3</sub> and R-SrTiO<sub>3</sub> have null polarizations, and the  $\phi(\vec{k}_\perp)$  phase is trivial and vanishes for all  $\vec{k}_\perp$  points. On the other hand, under compressive strains, both systems develop electric polarizations. In the following, we chose an inplane lattice constant  $a=3.71\text{\AA}$ , and determine the polarization structure for NR-SrTiO<sub>3</sub> and R-SrTiO<sub>3</sub> by using the optimized atomic positions and cell shapes of each system. Since NR-SrTiO<sub>3</sub> and R-SrTiO<sub>3</sub> have different sizes of unit cells, their Brillouin zones (BZ) are illustrated in Fig.3(a) and (b), respectively. The triangles highlighted by thick lines in Fig.3(a) and (b) are the high-symmetry paths along which the  $\vec{k}_\perp$ -dependent polarization structure is examined. The calculated  $\phi(\vec{k}_\perp)$  phase structures are shown in Fig.3(c). To facilitate comparison, both polarization structures are shifted to make  $\phi(\Gamma) = 0$  at  $\Gamma$ ; meanwhile, the horizontal axis of  $\vec{k}_\perp$  distance in R-SrTiO<sub>3</sub> is rescaled by a factor of  $\sqrt{2}$  in Fig.3(c), such that the two polarization dispersions can be given in the same figure.

Inspection of the polarization structures in Fig.3(c) reveals: (i) The dispersion bandwidth in NR-SrTiO<sub>3</sub> ( $\sim 0.9$ ) is considerably larger than that in R-SrTiO<sub>3</sub> ( $\sim 0.4$ ). (ii) In NR-SrTiO<sub>3</sub>, the largest  $\phi(\vec{k}_\perp)$  contribution comes from the  $X_2$  point at the zone corner, while in R-SrTiO<sub>3</sub> the largest contribution is at  $M_1$  which is on the zone boundary. (iii) In NR-SrTiO<sub>3</sub>,  $X_1$  point is a saddle point, while in R-SrTiO<sub>3</sub> there is no saddle point. Furthermore, in R-SrTiO<sub>3</sub>,  $M_2$  is a local minimum and another local maximum appears along the  $M_2 - \Gamma$  line, which is not the case in NR-SrTiO<sub>3</sub>. As a result, the two polarization dispersion curves have rather different curvatures.

While the above differences in the polarization structure between NR-SrTiO<sub>3</sub> and R-SrTiO<sub>3</sub> are interesting, they are also puzzling. With some effort, we find two possible reasons that might be responsible for these differences. The first one is folding effect. It is known in band-structure calculations that when one changes the size of unit cell, there is band-folding effect. However, it is unclear whether the folding effect also exists for polarization dispersion. If the answer is yes, one may also desire to establish a rigorous proof on the existence of

such an effect, and better yet, to uncover the precise manner on how the  $\phi(\vec{k}_\perp)$  dispersion curve folds itself. The second possible reason is rotational effect. When octahedral rotation is allowed, the atom-atom interaction in R-SrTiO<sub>3</sub> is anticipated to be different from in NR-SrTiO<sub>3</sub>, which could alter the electron distribution and thus the polarization structure. In the following, we will determine and analyze the consequences of both effects.

## B. Folding effect

To determine the significance of each of the above two effects (i.e., folding effect and rotational effect), it is preferable to design an approach that is able to investigate each effect separately. We first investigate the folding effect, by conducting the following calculations in order to avoid deliberately the rotational effect so that the latter will not play a role. We begin with an LDA-optimized 5-atom cell for NR-SrTiO<sub>3</sub> at a given inplane lattice (the solid of which is to be denoted as NR5), and then double the size of cell and convert it into a 10-atom cell (the solid of which is to be denoted as NR10, once again without oxygen rotation). The atomic positions and the electron charge densities in NR5 before conversion and in NR10 after conversion are thus equivalent. Also note that there is no oxygen rotation in either NR5 or NR10; differences in polarization structure between these two solids thus come from the folding effect alone.

Fig.4(a) presents the polarization structures of NR5 and NR10, both at  $a=3.71\text{\AA}$ . One sees that the polarization structure of NR10 (empty triangles in Fig.4a) appears very different from that of NR5 (empty squares). In particular, (i) The bandwidth of the NR5 curve is about twice as large as the NR10 case. (ii) For NR5,  $X_2$  is the maximum, and  $X_1$  is a saddle point as we saw previously. However for NR10,  $M_1$  and  $M_2$  have similar  $\phi(\vec{k}_\perp)$  values, making the curve between  $M_1$  and  $M_2$  evidently flat. (iii) The curvatures are different in two solids. As a result, apparently no relationship could be found for the two polarization-dispersion curves at first glance. More disturbingly, one may also wonder whether the polarization structure is uniquely defined for a given crystal, or whether it is meaningful to make a sensible comparison on polarization dispersion. To answer this, we will establish a rigorous relationship between the two curves in Fig.4(a), using an analytical approach based on Wannier functions.

We start with the expression for the polarization phase structure [10],  $\phi(\vec{k}_\perp) =$

$\frac{2\pi}{c} \sum_{\vec{R}_\perp} \sum_{n=1}^M \int \vec{r}_\parallel W_n^*(\vec{r}) W_n(\vec{r} - \vec{R}_\perp) e^{i\vec{k}_\perp \cdot \vec{R}_\perp} d\vec{r}$ , where  $W_n(\vec{r})$  is the Wannier function of the solid defined as  $W_n(\vec{r} - \vec{R}) = \frac{\sqrt{N}\Omega}{(2\pi)^3} \int_{BZ} d\vec{k} e^{i\vec{k} \cdot (\vec{r} - \vec{R})} u_{nk}(\vec{r})$ . Subscript  $\parallel$  (or  $\perp$ ) in the equation means the projection component parallel (or perpendicular, respectively) to the direction of the considered polarization;  $\vec{R}_\perp$  thus refers to a lattice vector perpendicular to the direction of the polarization.  $M$  is the number of occupied bands in solid. By defining parameters

$$t(\vec{R}_\perp) = \frac{2\pi}{c} \sum_{n=1}^M \int \vec{r}_\parallel W_n^*(\vec{r}) W_n(\vec{r} - \vec{R}_\perp) d\vec{r}, \quad (2)$$

we then arrive at a concise and analytic expression for polarization structure,

$$\phi(\vec{k}_\perp) = \sum_{\vec{R}_\perp} t(\vec{R}_\perp) e^{i\vec{k}_\perp \cdot \vec{R}_\perp}. \quad (3)$$

Sum over  $\vec{R}_\perp$  in Eq.(3) should in principle been carried out to infinite distance. In practice, owing to the localization nature of Wannier functions in dielectric materials[19, 20], it is often sufficient to truncate  $\vec{R}_\perp$  within a few near neighbors (NNs).

To simplify the formulations, we will consider, for NR5, up to the 3rd nearest-neighbor interactions in Eq.(3), with parameters  $t_0$ ,  $t_1$ ,  $t_2$ , and  $t_3$  representing respectively the on-site, first NN (1NN), second NN (2NN), and third NN (3NN) Wannier-function interactions as schematically illustrated in Fig.1(c). On an equal footing, the same truncation distance is used for Wannier-function interactions in NR10 where cell size is doubled. However, we should point out that our final conclusion on folding effect is generally applicable and does not depend on the distance within which Wannier-function interactions are truncated. Furthermore, to avoid ambiguity, we will use  $\vec{R}'_\perp$  and  $\phi'$  for NR5, while we use  $\vec{R}_\perp$  and  $\phi$  for NR10. For NR5 within 3NN truncation,  $\vec{R}'_\perp$ s are  $\vec{R}'_\perp = (0,0)$  (on site);  $(\pm a, 0)$  and  $(0, \pm a)$  (1NNs);  $(\pm a, \pm a)$  (2NNs);  $(\pm 2a, 0)$  and  $(0, \pm 2a)$  (3NNs). With tetragonal symmetry, we can rewrite Eq.(3) as

$$\begin{aligned} \phi'(\vec{k}_\perp) = & t_0 + 2t_1[\cos(k_1 a) + \cos(k_2 a)] \\ & + 4t_2 \cos(k_1 a) \cos(k_2 a) + 2t_3[\cos(2k_1 a) + \cos(2k_2 a)], \end{aligned} \quad (4)$$

where  $k_1$  and  $k_2$  are the components of  $\vec{k}_\perp$ , namely  $\vec{k}_\perp = (k_1, k_2)$ .

For NR10, there are two sets of Wannier functions in one unit cell, one set being the same as those in NR5 and another set having identical shapes but displaced by the lattice vector  $\vec{a}'_1$  of NR5. Meanwhile, we denote the Wannier-interaction parameters in NR10 as  $T_i$

as schematically shown in Fig.1(d), to be distinguished from  $t_i$  in NR5. Within the same truncation distance as in NR5, we only need to consider in NR10 the interactions between Wannier functions up to 2NNs, where  $\vec{R}_\perp=(0,0)$  (on site);  $(\pm a,\pm a)$  (1NNs);  $(\pm 2a,0)$  and  $(0,\pm 2a)$  (2NNs). The polarization structure in NR10 could be determined as

$$\begin{aligned} \phi(\vec{k}_\perp) = & T_0 + 4T_1 \cos(k_1 a) \cos(k_2 a) \\ & + 2T_2 [\cos(2k_1 a) + \cos(2k_2 a)] . \end{aligned} \quad (5)$$

By the definition of Eq.(2), it can be further shown that  $t_i$ s in NR5 and  $T_i$ s in NR10 are related by  $T_0 = 2t_0$ ,  $T_1 = 2t_2$ , and  $T_2 = 2t_3$ , since the Wannier functions are identical in both systems. Combining Eq.(4) with Eq.(5), one can find the following relation between  $\phi$  and  $\phi'$  phases

$$\phi(\vec{k}_\perp) = \phi'(\vec{k}_\perp) + \phi'(\vec{k}_\perp - \vec{b}_2) , \quad (6)$$

where  $\vec{b}_2 = \frac{\pi}{a}(\vec{i} + \vec{j})$  is one of the reciprocal lattice vectors of NR10. In other words, for an arbitrary  $\vec{k}_\perp$  point within the triangle  $\Gamma M_1 M_2$  in the irreducible BZ of NR10, the phase angle  $\phi(\vec{k}_\perp)$  of NR10 could be determined from the  $\phi'$  phases of NR5, at two  $\vec{k}_\perp$  points within the triangle  $\Gamma X_1 X_2$  in the irreducible BZ—one contribution being at the same  $\vec{k}_\perp$  point (the first term in Eq.6) and the other is the folded contribution at the  $\vec{k}_\perp - \vec{b}_2$  point (the second term in Eq.6). We thus prove that the folding effect indeed exists for the polarization dispersion structure.

We next would like to numerically confirm the validity of Eq.(6). We apply Eq.(6) and use the right-hand side of this equation to determine the polarization structure  $\phi(\vec{k}_\perp)$  of NR10. The results are given as solid squares in Fig.4(a), where we see that the analytic results of Eq.(6) coincide with those LDA calculated results of NR10. This demonstrates that the polarization structures of NR5 and NR10, although quite different looking, are equivalent and are thus physically meaningful.

### C. Rotational Effect

After revealing the existence of folding effect, we proceed to investigate rotational effect. To single out the rotation effect, we compare in Fig.4(b) the polarization structures of NR10 (without rotation) with that of R-SrTiO<sub>3</sub> (with rotation), both at the inplane lattice constant  $a=3.71\text{\AA}$ . Note that both systems have 10 atoms in one unit cell, and the folding effect is irrelevant here.

After eliminating the folding effect, we see in Fig.4(b) that the bandwidths of the polarization structures with and without rotation become notably similar. However, the two polarization structures still show important differences: (i)  $\phi(M_2)$  is a global maximum in non-rotational NR10, whereas being a local minimum in rotational structure; (ii)  $\phi(M_1)$  is still a saddle point in NR10 as in NR5, but is a global maximum in rotational case; (iii) Between  $M_1$  and  $M_2$ , very little dispersion exists for the polarization structure of NR10, which is not the case for R-SrTiO<sub>3</sub> where sizeable dispersion is evident; (iv) A local maximum is observed along  $M_2 - \Gamma$  in R-SrTiO<sub>3</sub>, and such a maximum does not exist in the case of NR10. Rotation of the oxygen octahedra alters the interactions among atoms (also the Wannier functions), which is responsible for the above-described differences in polarization structure. Differences (i)-(iv) also reveal that polarization structure is sensitive to the subtle changes in atomic positions and crystal structure, and could be used as an effective tool for studying material properties.

#### D. Response of polarization structure to in-plane strain

Compressive inplane strains—caused by lattice mismatch between epitaxially grown solid and substrate—modify interatomic interactions in an anisotropic fashion, by strengthening the interaction along inplane directions but weakening the interaction along the out-of-plane direction. This modification affects the structural and electric properties. As a consequence of the altered interatomic interaction, the polarization structure might also change accordingly. In this part, we examine the strain dependence of the polarization structure in R-SrTiO<sub>3</sub> with octahedral rotation, and contrast it with that in the non-rotational structure. To eliminate the folding effect, we use a unit cell of 10 atoms for non-rotational SrTiO<sub>3</sub> (i.e., NR10), same as for R-SrTiO<sub>3</sub>. The  $\vec{k}_\perp$  points are along the  $\Gamma \rightarrow M_1 \rightarrow M_2 \rightarrow \Gamma$  path as in Fig.3(b). The calculated polarization structures at different in-plane lattice constants are shown in Fig.5. More specifically, for R-SrTiO<sub>3</sub>, its polarization dispersions under different inplane  $a$  lattice constants are shown in Fig.5(a), while Fig.5(b) summarizes the phase  $\phi(\vec{k}_\perp)$  angles at high-symmetric  $M_1$  and  $M_2$  points as a function of the inplane lattice constant. For non-rotational NR10 structure, the polarization dispersions are given in Fig.5(c) while phase angles at  $M_1$  and  $M_2$  are summarized in Fig.5(d).

Let us focus on R-SrTiO<sub>3</sub> first. In Fig.5(a), we see that with the increase of in-plane

strain, the polarization structures change as following: (i) At zero strain or  $a=3.86\text{\AA}$ , the polarization  $\phi(\vec{k}_\perp)$  phase vanishes at all  $\vec{k}_\perp$  points, as a result of the existing inversion symmetry; (ii) Upon application of small strain, the bandwidth of polarization structure begins to increase. For  $3.83\text{\AA} \geq a \geq 3.71\text{\AA}$ , the  $\phi(\vec{k}_\perp)$  angle peaks at  $M_1$ , while being a local minimum at  $M_2$ . Meanwhile, a local maximum is observed along  $M_2$ - $\Gamma$ . On the other hand, the zone center,  $\Gamma$ , contributes the least to the total electronic polarization; (iii) When  $3.71\text{\AA} \geq a \geq 3.65\text{\AA}$ ,  $\phi(M_2)$  increases while  $\phi(M_1)$  slightly decreases, making the  $\phi(\vec{k}_\perp)$  curve of  $a=3.65\text{\AA}$  notably flat between  $M_1$  and  $M_2$ . (iv) As  $a$  is further decreased below  $3.65\text{\AA}$ ,  $M_2$  turns into the maximum point, while  $M_1$  becomes a saddle point. Meanwhile, the local maximum previously existing along  $M_2$ - $\Gamma$  disappears. Quantitatively, evolutions of the  $\phi(\vec{k}_\perp)$  phases at  $M_1$  and  $M_2$  with the inplane lattice constant are better visualized in Fig.5(b). The evolution can be separated into three regions: Region I where  $\phi(M_1)$  and  $\phi(M_2)$  both increase with the increasing strain, Region II where  $\phi(M_1)$  starts to decline but  $\phi(M_1)$  still contributes greater than  $\phi(M_2)$ , and Region III where crossover between  $\phi(M_1)$  and  $\phi(M_2)$  occurs and  $\phi(M_2)$  now becomes the maximum contribution.

The differences between R-SrTiO<sub>3</sub> and NR10, in their responses of polarization structure to inplane strain, can be seen by comparing Fig.5(d) with Fig.5(b), which yields the following observations: (i) When  $a$  is near  $3.83\text{\AA}$ ,  $\phi(M_1)$  and  $\phi(M_2)$  both increase linearly in R-SrTiO<sub>3</sub> [Fig.5(b)], while they remain nearly zero in NR10 [Fig.5(d)]. It reveals once again a lack of critical inplane strain in R-SrTiO<sub>3</sub>. However, in NR10 without rotation,  $a$  need be below  $3.83\text{\AA}$  in order to produce sizable polarization. (ii) When  $3.83\text{\AA} \leq a \leq 3.74\text{\AA}$ ,  $\phi(M_2)$  increases quickly with strain both in R-SrTiO<sub>3</sub> and in NR10, but the increasing slope in NR10 [Fig.5(d)] is much larger than in R-SrTiO<sub>3</sub> [Fig.5(b)]. During this region of strain, the polarization in NR10 is more sensitive to the inplane strain with larger piezoelectric response than in R-SrTiO<sub>3</sub>, and microscopically  $\phi(M_2)$  is largely responsible. (iii) Although the responses in Fig.5(d) can also be divided into three stages I, II and III for NR10, the inplane lattice constants delimiting the boundary of different stages differ, however, from those in Fig.5(b). (iv) In NR10,  $\phi(M_1)$  declines sharply at stages II and III, and as a result,  $\phi(M_2)$  becomes dominating when  $a \leq 3.68\text{\AA}$ . In R-SrTiO<sub>3</sub>,  $\phi(M_1)$  declines much slowly at stages II and III. (v)  $\phi(M_2)$  in NR10 reaches its maximum around  $a=3.65\text{\AA}$ , then starts to decrease. In R-SrTiO<sub>3</sub>,  $\phi(M_2)$  nevertheless keeps increasing.

Response of polarization structure to inplane strain is thus found interestingly different

in R-SrTiO<sub>3</sub> with oxygen rotation as compared to that in NR10 without rotation. These differences should, on the microscopic level, originate from the different interaction among the Wannier functions in two structures. In the following, we will extract from the polarization structure the interactions among Wannier functions.

### E. Implication on interaction between Wannier functions

Our procedure of determining Wannier-function interaction begins with Eq.(5), which was derived for crystals consisting of 10 atoms in one unit cell, and is thus applicable to both R-SrTiO<sub>3</sub> and NR10 though with different interaction parameters. Applying Eq.(5) to  $\phi(\vec{k}_\perp)$  at special  $\vec{k}_\perp$  points at  $\Gamma$ ,  $M_1$  and  $M_2$ , we obtain  $\phi(M_1) - \phi(\Gamma) = -4T_1 - 8T_2$  and  $\phi(M_2) - \phi(\Gamma) = -8T_1$ . From  $\phi(M_1)$  and  $\phi(M_2)$ , one can thus determine  $T_1$  and  $T_2$  quantities. As shown in Fig.1(d),  $T_1$  (or  $T_2$ ) corresponds to the Wannier-function interaction between a given cell with the 1st (or 2nd) neighboring cell, manifesting interatomic interaction on microscopic level. The obtained  $T_1$  and  $T_2$  quantities are then used in Eq.(5) to determine analytically the whole polarization dispersion curve. Note that only  $\phi$  phases at  $M_1$  and  $M_2$  points are fitted. To evaluate the validity of our analytic formulas, we choose three inplane lattice constants across the entire strain range considered in this work, and plot the *analytic* polarization dispersions as open symbols in Fig.6(a) for R-SrTiO<sub>3</sub> and in Fig.6(b) for NR10. One sees that for each inplane lattice constant, the polarization structures analytically determined from Eq.(5), and the direct results obtained from the Berry-phase modern theory of polarization, agree well. More specifically, for the  $a=3.80\text{\AA}$  curve in Fig.6(a), the small dispersion hump between  $M_2$  and  $\Gamma$  is well reproduced by analytical result. Furthermore, at  $a=3.59\text{\AA}$  which is a more stringent test on the analytic formulation with truncated interaction, the saddle-point nature at  $M_1$  in Fig.6(a), as well as the subtle minimum at  $M_1$  in Fig.6(b), are also predicted by the analytic expressions. These demonstrate the validity of our analytic formulation; the obtained  $T_1$  and  $T_2$  values are thus reliable.

The obtained  $T_1$  and  $T_2$  quantities are given in Table II and shown in Fig.6(c) and (d). One can see from Fig.6(c) and (d) that, for a given inplane lattice constant,  $T_i$  is notably different in R-SrTiO<sub>3</sub> with respect to that in non-rotational NR10. For instance, at  $a=3.68\text{\AA}$ ,  $T_1$  in NR-SrTiO<sub>3</sub> is  $\sim 50\%$  larger than in R-SrTiO<sub>3</sub>, and  $T_2$  in NR-SrTiO<sub>3</sub> even has a different sign from  $T_2$  in R-SrTiO<sub>3</sub>. These quantitative differences in microscopic interactions indicate

that polarization structure is indeed a rather powerful tool to understand physical properties. We also note that, at large inplane strain such as  $a=3.59\text{\AA}$ ,  $T_2$  is large in NR-SrTiO<sub>3</sub> but nearly vanishes in R-SrTiO<sub>3</sub> [Fig.6(d)], implying that interactions in rotational and non-rotational structures are significantly different. Furthermore, we observe that at very small inplane lattice constants near  $a=3.59\text{\AA}$ ,  $T_1$  and  $T_2$  tend to saturate in NR-SrTiO<sub>3</sub> but not in R-SrTiO<sub>3</sub>.

### F. Determination of higher-order Wannier-function interaction

One relevant question in the theory of polarization structure is the determination of the  $t_i$ s quantities, particularly those higher-order  $t_i$ s that correspond to larger  $\vec{R}_\perp$ s, since by knowing  $t_i$ s the  $\phi(\vec{k}_\perp)$  phases can be readily obtained via Eq.(3). The  $t_i$  quantities connect the microscopic interaction with macroscopic  $\vec{k}_\perp$ -dependent polarization structure. As one useful outcome of the current study, we describe an approach that can be utilized to determine the higher-order  $t_i$  interactions.

The approach works in general. But for the sake of convenience in our discussion, we will take NR-SrTiO<sub>3</sub> (without oxygen rotation) of  $a=3.59\text{\AA}$  as an example. For NR-SrTiO<sub>3</sub>, the smallest unit cell consists of 5 atoms, and the polarization structure directly calculated from Berry phase is given in Fig.7. Now if we use a lower-order 2NN approximation in Eq.(3), with interactions  $t_0$ ,  $t_1$  and  $t_2$  in Fig.1(c), to analytically mimic the polarization structure, it is easy to derive that the polarization structure will be  $\phi(\vec{k}_\perp) = t_0 + 2t_1[\cos(k_1a) + \cos(k_2a)] + 2t_2[\cos(k_1 + k_2)a + \cos(k_1 - k_2)a]$ . By using the phase angles at  $\Gamma$ ,  $X_1$  and  $X_2$  points, one can determine  $t_0$ ,  $t_1$  and  $t_2$ . The polarization dispersion within the 2NN approximation can be subsequently obtained and is given in Fig.7. One sees that the agreement between the directly calculated polarization curve and the 2NN-approximated curve is not good. For instance,  $\phi(X_2)$  is incorrectly predicted by the 2NN approximation to be a local minimum, instead of a local maximum as by the direct calculation. Meanwhile, the dispersion curvatures along  $X_1$ - $X_2$  and along  $X_2 - \Gamma$  are wrong. We thus see that higher-order interactions among Wannier functions are needed. This is not surprising, since at small inplane lattice constants, interactions between farther neighboring cells remain strong and can not be neglected.

To determine higher-order  $t_i$  quantities, one possible approach (denoted as approach I)

is to use higher-order  $\phi(\vec{k}_\perp)$  expression such as Eq.(4) within the 3NN approximation, and in Eq.(4) four  $t_i$ s need be fitted. In this approach, if even higher-order approximations than 3NN are used, more  $t_i$ s have to be fitted at many  $\vec{k}_\perp$  points, which becomes increasingly complex and less trackable. An alternative approach (denoted as approach II) is the following. First, we recognize from the finding of the folding effect in Sec.IIIB that, when one doubles the size of unit cell from 5-atoms to 10-atoms, the solid is the same, but the  $t_1$  term drops as seen by comparing Eq.(5) with Eq.(4). As a result, one is still left with three (not four) parameters, and can be determined by fitting  $\phi(\vec{k}_\perp)$ s at three  $\vec{k}_\perp$  points. Similarly, one can determine even higher-order Wannier-function interactions by varying the size of unit cell. In fact, when one increases the size of unit cell (doubling, tripling, etc), the interactions between those Wannier functions—that are located in different cells of previously smaller cell size but fall in the same cell of the larger cell size—are dropped. As a result, with the large unit cell, determination of new Wannier-function interactions becomes simplified, which corresponds to higher-order NN interactions with respect to the previous smaller unit cell. For instance, in Eq.(5) when cell size is doubled, a new interaction parameter  $T_2$  (i.e.,  $t_3$  since  $T_2 = 2t_3$ ) is determined. This approach is, in spirit, similar to the renormalization-group (RG) approach used in understanding critical behaviors of phase transition [21]. Of course, the benefit of approach II is at the expense of computing the Berry-phase polarization structure in larger unit cell, but the increase of computation is rather small.

To examine how approach II works, we give in Fig.7 the analytical dispersion determined within the 3NN approximation, with  $t_1$  obtained from 5-atom-cell calculation, and with  $t_2$  and  $t_3$  obtained from 10-atom-cell calculation. The obtained values are  $t_1=-3.590\times 10^{-2}$ ,  $t_2=-2.711\times 10^{-2}$ , and  $t_3=1.761\times 10^{-2}$ . As one could easily see from Fig.7, inclusion of  $t_3$  interaction in the 3NN approximation yields a much better dispersion than the 2NN one. The local-maximum nature at  $X_2$ , the characteristic dip between  $X_1$  and  $X_2$ , and the curvature between  $X_2$  and  $\Gamma$  in the direct Berry-phase calculation results are well described by the 3NN approximation but not the 2NN approximation.

#### IV. SUMMARY

Polarization structure in R-SrTiO<sub>3</sub> with rotational instability is studied, and contrasted with the dispersion in NR-SrTiO<sub>3</sub> where oxygen-octahedra rotation is deliberately not allowed by symmetry constraint. Influences of in-plane compressive strains on the polarization dispersion as well as on the phase contributions at high-symmetric  $\vec{k}_\perp$  points are investigated. Microscopic interactions are deduced by means of Wannier-function formulation, and the dependencies of  $T_1$  and  $T_2$  interactions on the inplane strain are determined.

Our specific findings are summarized as following: (i) The polarization structures of ST with and without oxygen rotation, at the same in-plane lattice constant, are rather different. These differences could be attributed to two reasons, the folding effect and the rotational effect. (ii) We have proved, both numerically and analytically via the Wannier-function formulation, that folding effect exists in polarization structure. As a result, polarization structures are equivalent for differently chosen unit cells, and are thus physically meaningful. We also reveal how polarization structure folds itself. (iii) After elimination of folding effect by choosing the same unit cell, the polarization structures for rotational and non-rotational geometries have similar bandwidth. But the dispersion curvatures and individual  $\phi(\vec{k}_\perp)$  phases are still considerably different as shown in Fig.4(b), which reveals that polarization structure is sensitive to the structure distortion and is indeed an effective tool to study materials properties of dielectrics. (iv) With application of in-plane compressive strain, the  $\phi(\vec{k}_\perp)$  phase at high-symmetric  $M_1$  point is found to decline sharply at stage III in NR-SrTiO<sub>3</sub> [Fig.5(d)], and in contrast, the decline is much slower in R-SrTiO<sub>3</sub> [Fig.5(c)]. Furthermore, in NR-SrTiO<sub>3</sub>, the  $\phi(\vec{k}_\perp)$  phase at another high-symmetric  $M_2$  point first increases at small strain and then declines at high strain. However, in R-SrTiO<sub>3</sub>, the  $\phi$  phase at  $M_2$  keeps increasing throughout the considered strain range. (v) From polarization structure, we obtained the microscopic  $T_1$  and  $T_2$  interactions as given in Fig.6(c) and (d).  $T_i$  interaction is found to differ significantly in R-SrTiO<sub>3</sub> and NR-SrTiO<sub>3</sub>. Moreover,  $T_2$  in Fig.6(d) is revealed to exhibit an interesting non-monotonous dependence on inplane lattice constant. (vi) We have further described a renormalization-like method to determine higher-order Wannier-function interactions by varying the size of unit cell. We revealed that the 3NN approximation is necessary for an accurate description of the polarization structure of NR-SrTiO<sub>3</sub> at  $a=3.59\text{\AA}$ .

## V. ACKNOWLEDGEMENT

This work is supported by the Office of Naval Research.

---

- [1] H. Uwe and T. Sakudo, Phys. Rev. B **13**, 271 (1976).
- [2] K. A. Muller, W. Berlinger, M. Capizzi, and M. Granicher, Solid State Commun. **8**, 549 (1970).
- [3] C. J. Fennie and K. M. Rabe, Phys. Rev. B **72**, 100103 (2005).
- [4] N. Sai, C. J. Fennie, and A. A. Demkov, Phys. Rev. Lett. **102**, 107601 (2009).
- [5] I. I. Mazin and D. J. Singh, Phys. Rev. B **56**, 2556 (1997).
- [6] Z. Fang and K. Terakura, Phys. Rev. B **64**, 020509 (2001).
- [7] N. Ray and U. V. Waghmare, Phys. Rev. B **77**, 134112 (2008).
- [8] R. D. King-Smith and D. Vanderbilt, Phys. Rev. B **47**, 1651 (1993).
- [9] R. Resta, Rev. Mod. Phys. **66**, 889 (1994).
- [10] Y. Yao and H. Fu, Phys. Rev. B **79**, 014103 (2009).
- [11] A. Antons, J. B. Neaton, K. M. Rabe, and D. Vanderbilt, Phys. Rev. B **71**, 024102 (2005).
- [12] P. Hohenberg and W. Kohn, Phys. Rev. **136**, B864 (1964); W. Kohn and L.J. Sham, Phys. Rev. **140**, A1133 (1965).
- [13] N. Troullier and J. L. Martins, Phys. Rev. B **43**, 1993 (1991).
- [14] H. Fu and O. Gulseren, Phys. Rev. B **66**, 214114 (2002); H. Fu, in *Fundamental Physics of Ferroelectrics*, p. 17 (AIP, Melville, 2002), edited by R. E. Cohen.
- [15] Details were given in Ref.14 and in I. Naumov and H. Fu, Phys. Rev. B **72**, 012304 (2005).
- [16] T. Mitsui, M. Adachi, J. Harada, T. Ikeda, S. Nomura, E. Sawguchi, and T. Yamada, in “*Landolt-Bornstein Numerical Data and Functional Relationships in Science and Technology: Oxides*”, New Series, Group III, Vol. 16, Pt. a (Springer-Verlag, Berlin, 1979).
- [17] E. Courtens, Phys. Rev. Lett. **29**, 1380 (1972).
- [18] N. Sai and D. Vanderbilt, Phys. Rev. B **62**, 13942 (2000).
- [19] J. Des Cloizeaux, Phys. Rev. **135**, A698 (1964).
- [20] N. Marzari and D. Vanderbilt, Phys. Rev. B **56**, 12847 (1997).
- [21] K. G. Wilson, Rev. Mod. Phys. **47**, 773 (1975).

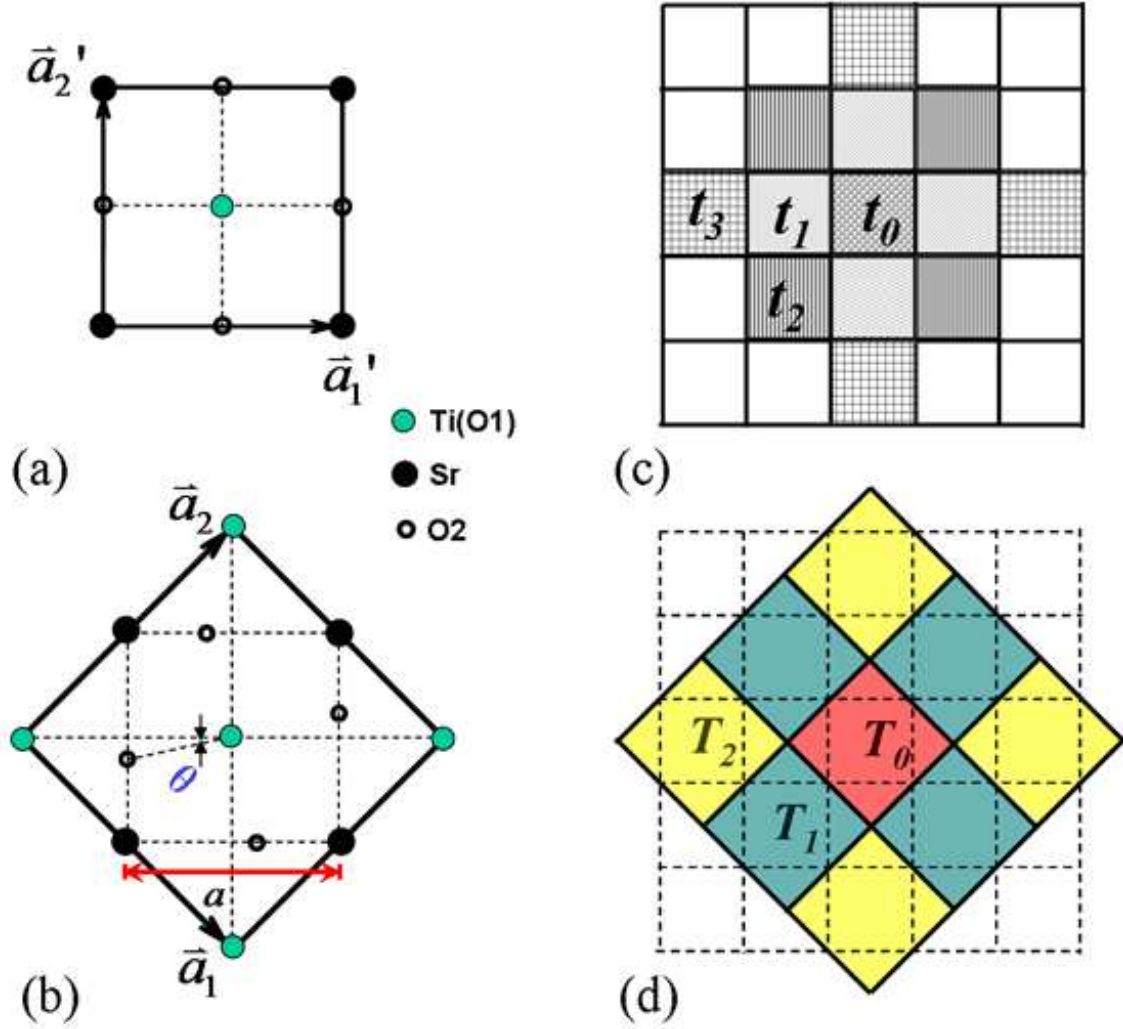


FIG. 1: (Color online) (a) Top view along the [001] direction of the 5-atom cell, for SrTiO<sub>3</sub> without oxygen-octahedra rotation. (b) Top view of the 10-atom cell for SrTiO<sub>3</sub> with oxygen rotation. (c) Schematic illustration of the interaction between Wannier functions in different cells, for NR-SrTiO<sub>3</sub> consisting of 5-atom cells. (d) Similar as (c), but for R-SrTiO<sub>3</sub> consisting of 10-atom cells.

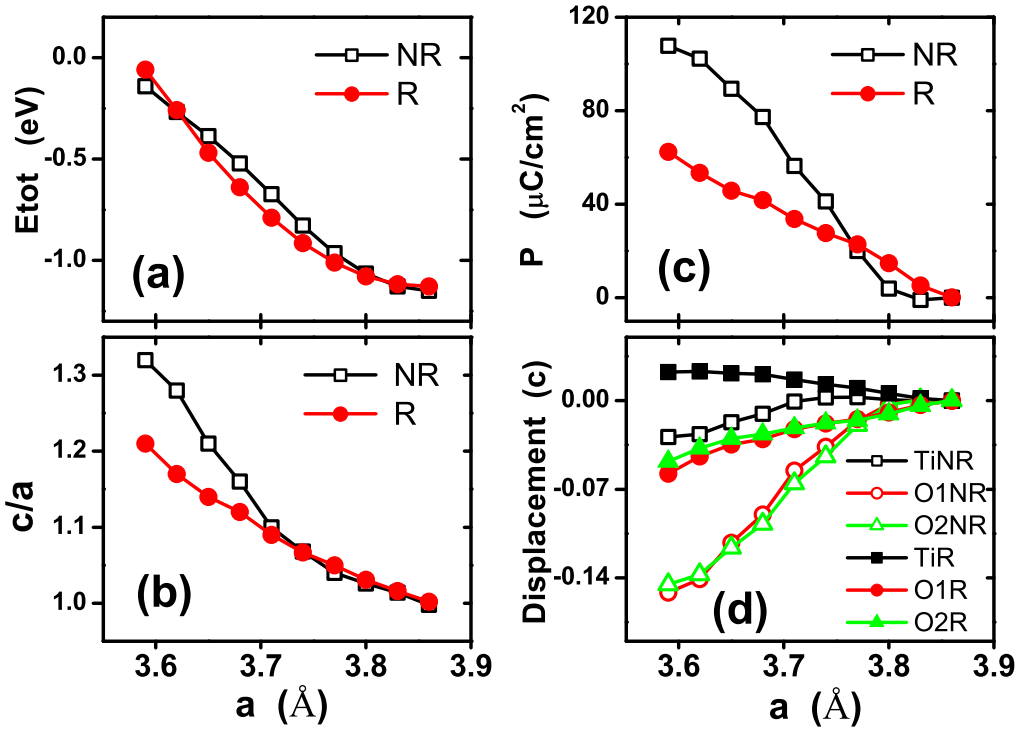


FIG. 2: (Color Online) The following calculated properties as a function of the in-plane  $a$  lattice constant in R-SrTiO<sub>3</sub> and NR-SrTiO<sub>3</sub>: (a) total energy of a 10-atoms cell (with respect to a basis of -7474 eV), (b) the  $c/a$  tetragonality, (c) the total (electronic and ionic) polarization, (d) atomic displacements along the  $c$ -axis. Atomic displacements in (d) are obtained by comparing the LDA-optimized atomic positions with respect to the high-symmetric locations. High-symmetric locations are defined as: we first shift the Sr atom to the origin of the coordinate, and then the high-symmetric atomic positions are  $z = 0$  for Sr and O1 atoms, and  $z = \frac{c}{2}$  for Ti and O2 atoms. O1 is apical while O2 is on the base plane of an octahedra.

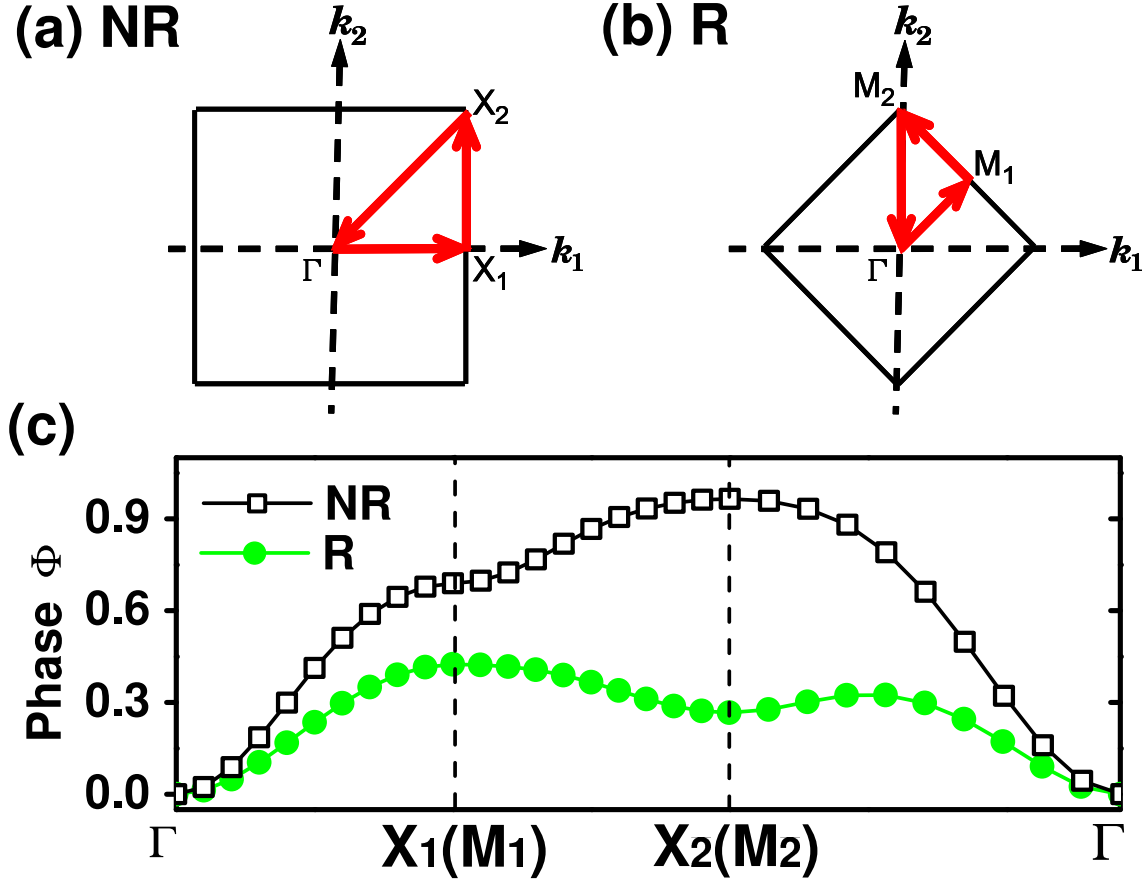


FIG. 3: (a) The two-dimensional Brillouin zone over which  $\vec{k}_\perp$  is sampled, for NR-SrTiO<sub>3</sub> with five atoms in one cell. (b) The two-dimensional Brillouin zone over which  $\vec{k}_\perp$  is sampled, for R-SrTiO<sub>3</sub> with ten atoms in one cell. (c) Polarization structures of NR-SrTiO<sub>3</sub> and R-SrTiO<sub>3</sub>, both at  $a=3.71\text{\AA}$ . For NR-SrTiO<sub>3</sub>, 5-atom cell is used for the polarization structure calculation. For R-SrTiO<sub>3</sub>, the horizontal  $\vec{k}_\perp$  distance is rescaled by a factor of  $\sqrt{2}$  such that its dispersion structure and the counterpart of NR-SrTiO<sub>3</sub> can be plotted in the same figure.

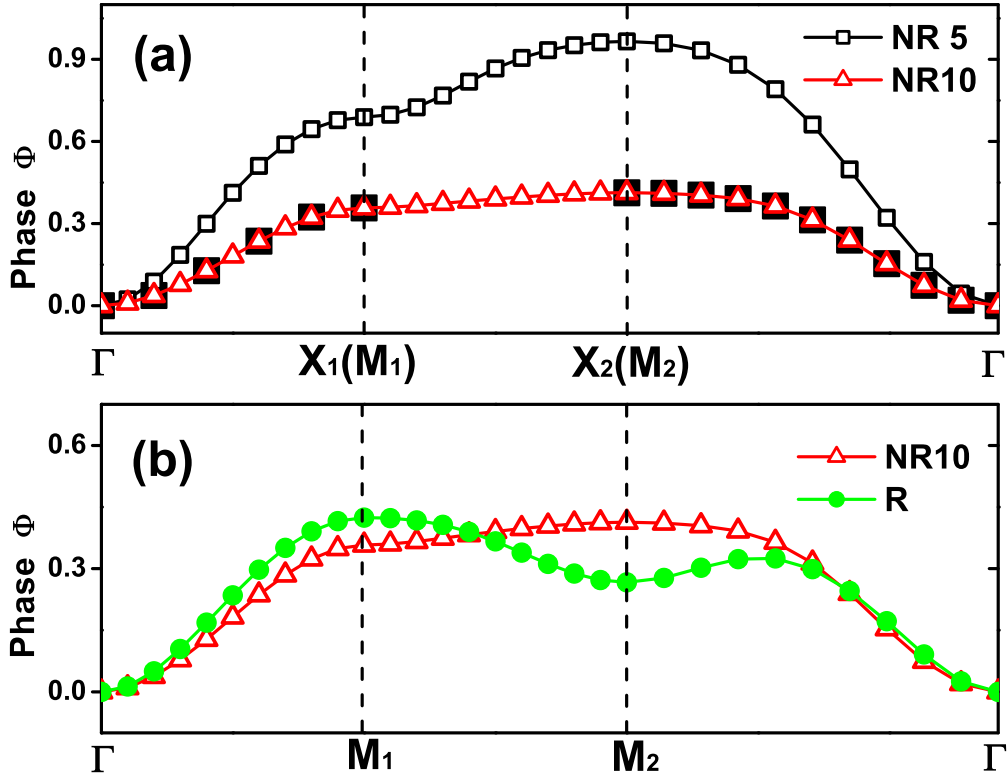


FIG. 4: (a) Polarization structures of NR5 and NR10 at inplane lattice constant  $a=3.71\text{\AA}$ . The analytic result using Eq.(6) is also shown as solid squares. (b) Comparison between the polarization structure of NR10 and that of R-SrTiO<sub>3</sub> at  $a=3.71\text{\AA}$ .

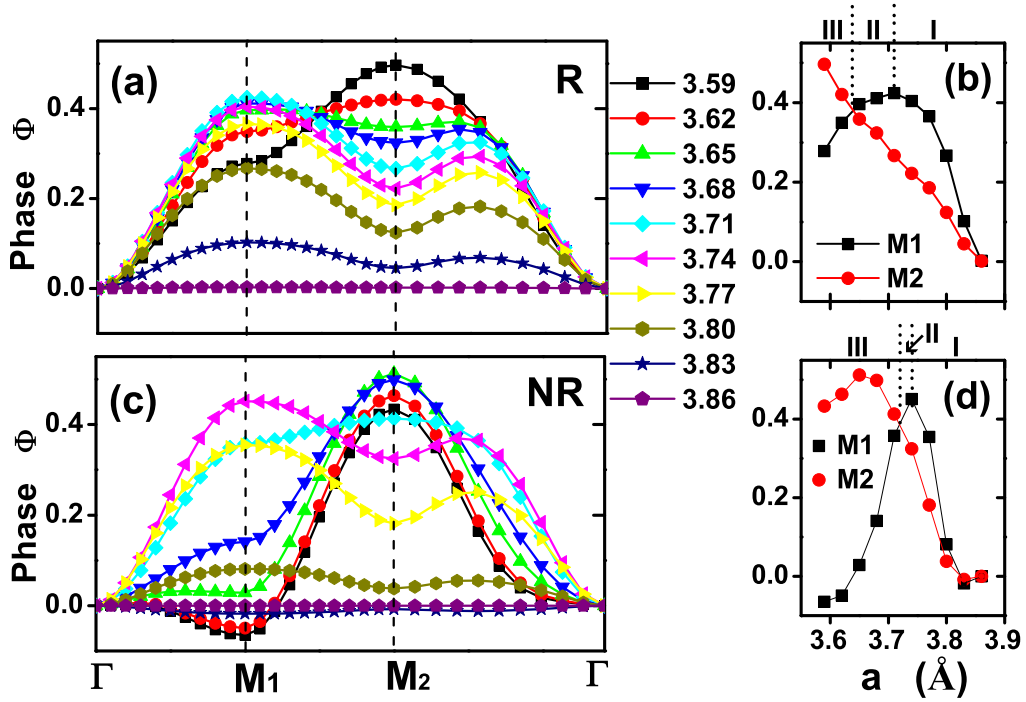


FIG. 5: (Color online) (a) Polarization structure of R-SrTiO<sub>3</sub> at different in-plane lattice constants; (b) Phase angles at  $M_1$  and  $M_2$  as a function of the in-plane  $a$  lattice constant, for R-SrTiO<sub>3</sub>. (c) Polarization structure of non-rotational NR10 at different in-plane lattice constants; (d) Phase angles at  $M_1$  and  $M_2$  as a function of the in-plane  $a$  lattice constant, for NR10. All polarization dispersion curves are rigidly shifted such that  $\phi(\Gamma) = 0$  for the sake of comparison.

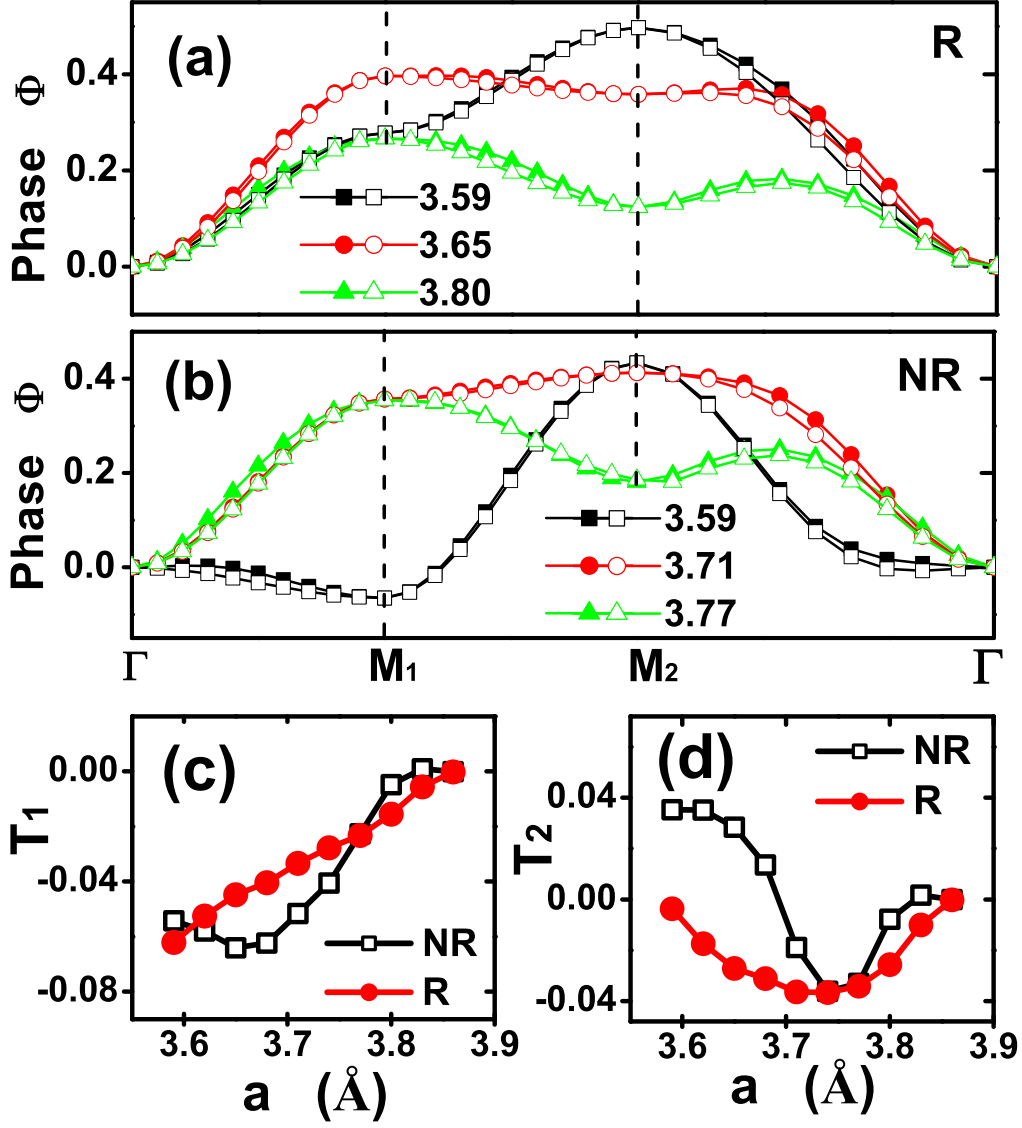


FIG. 6: (a) Analytic polarization dispersions (open symbols) determined from Eq.(5), as compared to the direct results (filled symbols) calculated from the modern theory of polarization, for R-SrTiO<sub>3</sub> at inplane lattice constants  $a=3.80$ ,  $3.65$ , and  $3.59$ Å. Lines are guides for eyes. Since analytic results agree well with direct calculation results, most of open symbols are on top of filled symbols. (b) Similar as (a), but for NR10 at  $a=3.77$ ,  $3.71$ , and  $3.59$ Å. (c) Dependence of the  $T_1$  quantity on the inplane  $a$  lattice constant, for R-SrTiO<sub>3</sub> and NR10. (d) Dependence of the  $T_2$  quantity on the inplane lattice constant.

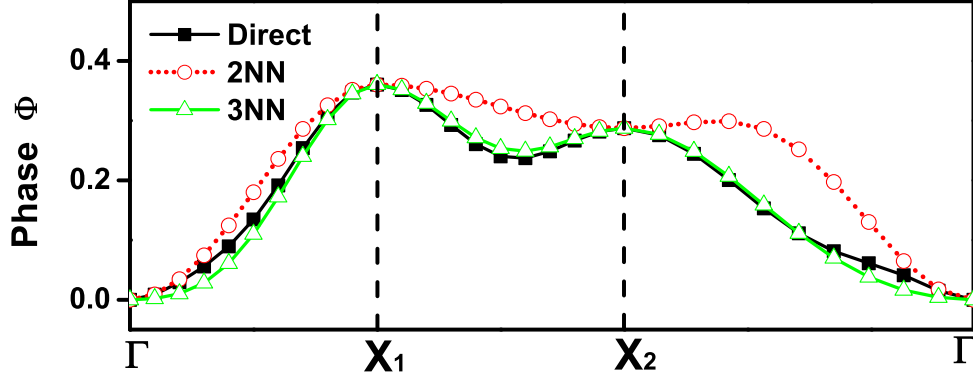


FIG. 7: Polarization structure of NR-SrTiO<sub>3</sub> at  $a=3.59\text{\AA}$  computed from direct Berry Phase calculation (solid squares), 2NN approximation (open circles and dotted line), and 3NN approximation (open triangles). Lines are guides for eyes.

TABLE I: The LDA-optimized  $c/a$  ratios for NR-SrTiO<sub>3</sub> and R-SrTiO<sub>3</sub> under different inplane lattice constants. For R-SrTiO<sub>3</sub>, the calculated rotation angle is also given.

$a(\text{\AA})$	NR-SrTiO <sub>3</sub>	R-SrTiO <sub>3</sub>	
	$c/a$	$c/a$	angle $\theta(^{\circ})$
3.59	1.32	1.21	12.70
3.62	1.28	1.17	12.31
3.65	1.21	1.14	11.71
3.68	1.16	1.12	10.92
3.71	1.10	1.09	9.95
3.74	1.068	1.067	8.80
3.77	1.040	1.050	7.81
3.80	1.026	1.031	6.57
3.83	1.014	1.016	5.39
3.86	0.998	1.002	3.25

TABLE II:  $T_1$  and  $T_2$  quantities (in radian) at different inplane lattice constants.

$a$ (Å)	NR10		R-SrTiO <sub>3</sub>	
	$T_1$ ( $10^{-2}$ )	$T_2$ ( $10^{-2}$ )	$T_1$ ( $10^{-2}$ )	$T_2$ ( $10^{-2}$ )
3.59	-5.422	3.522	-6.210	-0.372
3.62	-5.798	3.512	-5.256	-1.736
3.65	-6.408	2.842	-4.848	-2.714
3.68	-6.234	1.350	-4.064	-3.116
3.71	-5.162	-1.888	-3.334	-3.636
3.74	-4.058	-3.612	-2.780	-3.662
3.77	-2.272	-3.298	-2.322	-3.412
3.80	-0.476	-0.778	-1.552	-2.562
3.83	9.74E-2	1.74E-1	-0.562	-0.998